

# Optimization of dual-energy CT acquisitions for proton therapy using projection-based decomposition

Gloria Vilches-Freixas, Jean Michel Létang, Nicolas Ducros, and Simon Rit<sup>a)</sup>

*Université de Lyon, CREATIS, CNRS UMR5220, Inserm U1206, INSA-Lyon, Université Lyon 1, Centre Léon Bérard, Lyon, France*

(Received 3 March 2017; revised 21 June 2017; accepted for publication 26 June 2017; published 18 August 2017)

**Purpose:** Dual-energy computed tomography (DECT) has been presented as a valid alternative to single-energy CT to reduce the uncertainty of the conversion of patient CT numbers to proton stopping power ratio (SPR) of tissues relative to water. The aim of this work was to optimize DECT acquisition protocols from simulations of X-ray images for the treatment planning of proton therapy using a projection-based dual-energy decomposition algorithm.

**Methods:** We have investigated the effect of various voltages and tin filtration combinations on the SPR map accuracy and precision, and the influence of the dose allocation between the low-energy (LE) and the high-energy (HE) acquisitions. For all spectra combinations, virtual CT projections of the Gammex phantom were simulated with a realistic energy-integrating detector response model. Two situations were simulated: an ideal case without noise (infinite dose) and a realistic situation with Poisson noise corresponding to a 20 mGy total central dose. To determine the optimal dose balance, the proportion of LE-dose with respect to the total dose was varied from 10% to 90% while keeping the central dose constant, for four dual-energy spectra. SPR images were derived using a two-step projection-based decomposition approach. The ranges of 70 MeV, 90 MeV, and 100 MeV proton beams onto the adult female (AF) reference computational phantom of the ICRP were analytically determined from the reconstructed SPR maps.

**Results:** The energy separation between the incident spectra had a strong impact on the SPR precision. Maximizing the incident energy gap reduced image noise. However, the energy gap was not a good metric to evaluate the accuracy of the SPR. In terms of SPR accuracy, a large variability of the optimal spectra was observed when studying each phantom material separately. The SPR accuracy was almost flat in the 30–70% LE-dose range, while the precision showed a minimum slightly shifted in favor of lower LE-dose. Photon noise in the SPR images (20 mGy dose) had lower impact on the proton range accuracy as comparable results were obtained for the noiseless situation (infinite dose). Root-mean-square range errors averaged over all irradiation angles associated to dual-energy imaging were comprised between 0.50 mm and 0.72 mm for the noiseless situation and between 0.51 mm and 0.77 mm for the realistic scenario.

**Conclusions:** The impact of the dual-energy spectra and the dose allocation between energy levels on the SPR accuracy and precision determined through a projection-based dual-energy algorithm were evaluated to guide the choice of spectra for dual-energy CT for proton therapy. The dose balance between energy levels was not found to be sensitive for the SPR estimation. The optimal pair of dual-energy spectra was material dependent but on a heterogeneous anthropomorphic phantom, there was no significant difference in range accuracy and the choice of spectra could be driven by the precision, i.e., the energy gap. © 2017 American Association of Physicists in Medicine [<https://doi.org/10.1002/mp.12448>]

Key words: dual-energy CT, optimization protocol, proton range, proton therapy

## 1. INTRODUCTION

In proton treatment planning, the range of protons in patients is determined from the stopping power ratio (SPR) of tissues relative to water along the beam path. Multiple sources cause range uncertainty, in particular: patient setup errors, uncertainties in the conversion of X-ray CT numbers to proton SPR, beam delivery errors and dose calculation approximations.<sup>1</sup> In clinical practice, safety margins are added to the target volume to account for the uncertainty in predicting proton ranges in tissues. Unfortunately, the use of large margins prevents full benefit of proton therapy.<sup>1</sup>

The stoichiometric calibration proposed by Schneider et al. (1996)<sup>2</sup> has been widely adopted in the current practice to convert planning X-ray CT images into SPR maps based on single-energy CT (SECT). However, a 3.5% range uncertainty has been associated with this conversion.<sup>3</sup> Dual-energy CT (DECT), by exploiting the differences of X-ray attenuation coefficients of tissues at different energies, has the potential to reduce this uncertainty, and thus, to improve the range estimation.

There are different commercial strategies to perform DECT such as dual-source, fast kV-switching, dual-layer scanners, and photon-counting detectors.<sup>4</sup> DECT imaging

consists in recording two datasets of a given anatomical area at different X-ray voltages, or with one voltage but measuring different parts of the spectrum at the detector level. By combining these images, either in the projection domain (prior to image reconstruction)<sup>5,6</sup> or in the image domain (after image reconstruction),<sup>7–10</sup> one can characterize and segment the patient tissues. Relative electron density (RED) and effective atomic number ( $Z_{\text{eff}}$ ) are quantities commonly used for material segmentation in radiotherapy applications that can be estimated from DECT. SPR can then be derived from RED and  $Z_{\text{eff}}$  maps and the Bethe–Bloch equation,<sup>11</sup> or by establishing a polyline curve (RED, SPR/RED) through calibration.<sup>12</sup> Other SPR estimators from dual-energy outputs have been recently proposed in the literature which do not require the determination of the intermediate variable  $Z_{\text{eff}}$  with comparable results.<sup>13,14</sup>

There is a growing concern about the imparted doses in medical imaging applications, particularly for diagnostic procedures. By balancing the dose between the low- and the high-energy acquisitions, radiation dose levels of DECT imaging are not necessarily higher than those of SECT imaging.<sup>15</sup> Due to the additional information contained in DECT data compared to SECT, it seems also feasible to further reduce radiation doses with dual-energy imaging. For that, the optimization of DECT acquisition protocols focusing on the figure of merit specific for each task, e.g., diagnostic or radiotherapy treatment planning, is mandatory. In addition, a careful study of the influence of the various acquisition parameters on the accuracy of the extracted data is of importance. Spectral optimization of dual-energy imaging has been conducted for cardiac, chest, and mammography imaging applications.<sup>16–18</sup> Additional spectral filtration has been optimized to improve the dual-energy performance in material discrimination tasks based on the dual-energy ratio.<sup>19,20</sup> In most of these works, the optimization of DECT acquisition settings, i.e., dose distribution between low- and high-energy acquisitions, tube voltage pair, filter material, and thickness, is based on the contrast-to-noise ratio (CNR) or the signal-to-noise ratio (SNR) criterion. In a recent work,<sup>21</sup> a framework for optimizing spectral CT imaging parameters and hardware design with respect to material classification tasks has been proposed.

In this work, we have focused on investigating the effect of two factors, namely the dual-energy spectra and the dose balance between energy levels, to maximize the accuracy and the precision of SPR maps, which are figures of merit essential for proton therapy dose calculations. First, we have investigated the effect of various voltages and tin filtration combinations on the SPR. Second, holding the dose to the patient constant, we have studied the influence of the distribution of dose between the low- and the high-energy acquisitions on the reconstructed SPR images, using four representative dual-energy spectra. The SPR images of three slices of the Adult Female (AF) ICRP computational phantom (i.e., head, thorax, and pelvis) have been reconstructed for the same four pairs of spectra. Then, the ranges of a 70 MeV, 90 MeV, and a 100 MeV proton beam — which

corresponded to a range in water of 40.8 mm, 64.0 mm, and 77.2 mm, respectively — have been computed from the reconstructed SPR maps at different incident angles. The proton range accuracy of each setup has been estimated by calculating the mean range deviation over all irradiation angles and the root-mean-square (RMS) error. The gain in range accuracy, based on this dual-energy approach, has also been compared to a single-energy CT acquisition of the AF ICRP phantom at 120 kVp.

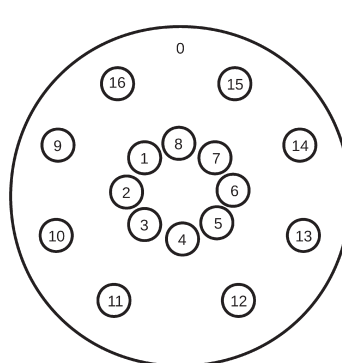
## 2. MATERIALS AND METHODS

### 2.A. Image simulation

The 33-cm diameter Gammex RMI 467 (Gammex, Middleton, WI, USA) tissue characterization phantom, which represents a medium-size body, was used to investigate the optimal dual-energy spectra and the optimal dose balance between energy levels. Sixteen inserts mimicking human tissue attenuation properties positioned as described in Fig. 1 with mass densities ranging from 0.3 to 1.82 g cm<sup>-3</sup> and known chemical compositions were considered. The index-to-material mapping and the reference SPR values are provided in Fig. 1.

The AF reference computational phantom of the International Commission on Radiological Protection (ICRP)<sup>22</sup> was used as a virtual patient to investigate the influence of the previous results on the proton range estimation. This phantom represents an average female and it contains 140 organs made of 53 standard human tissues, whose mass density and chemical composition are provided in the same ICRP Publication 110.<sup>22</sup> Each voxel has a dimension of 1.774 × 1.775 × 4.84 mm<sup>3</sup>. Three axial slices of different anatomical regions were selected to evaluate different human tissues and irradiation geometries: head, thorax, and pelvis (Fig. 2).

For both phantoms, the electron density relative to water of each insert material or tissue  $m$  was estimated using:



ID	Materials	SPR
0	Water	1.004
1	CB2-50% CaCO <sub>3</sub>	1.439
2	BR12 Breast	0.972
3	SB3 Cortical Bone	1.634
4, 15	AP6 Adipose	0.939
5, 14	LV1 Liver	1.072
6	BRN-SR2 Brain	1.071
7, 12	Solid Water	1.002
8, 9	LN300 Lungs	0.284
10	LN450 Lungs	0.431
11	CB2-30% CaCO <sub>3</sub>	1.271
13	IB3 Inner Bone	1.089
16	B200 Bone Mineral	1.098

Fig. 1. Left: Gammex 467 phantom. Right: insert ID, material name and reference SPR values.

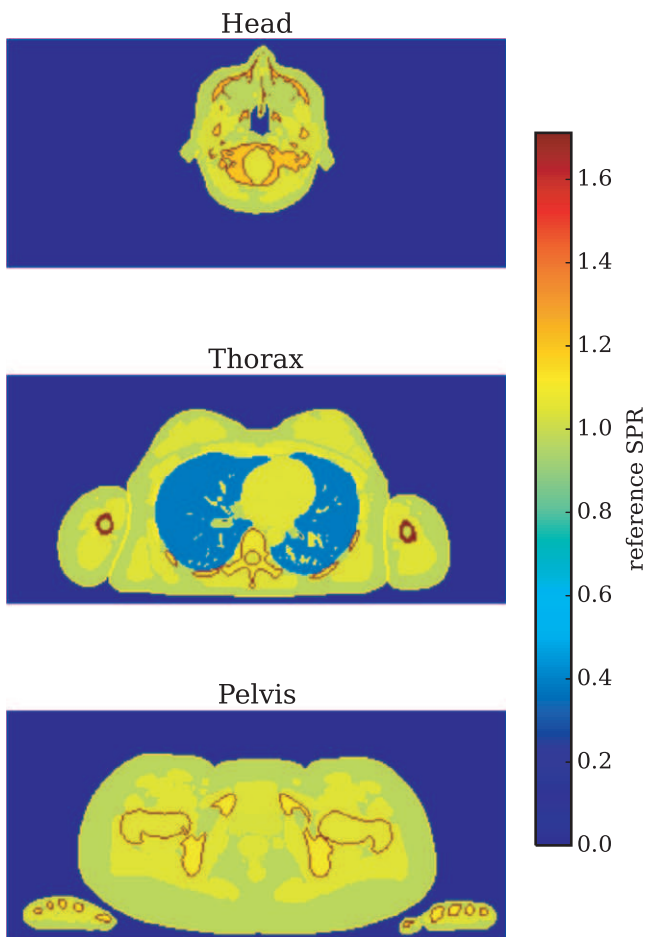


Fig. 2. Reference SPR images for the head, thorax, and pelvis slices of the AF ICRP phantom. [Color figure can be viewed at [wileyonlinelibrary.com](http://wileyonlinelibrary.com)]

$$RED_m = \frac{\rho_m \left[ \sum_i w_i \frac{Z_i}{A_i} \right]_m}{\rho_w \left[ \sum_i w_i \frac{Z_i}{A_i} \right]_w} \quad (1)$$

where the label  $w$  refers to water,  $\rho$  is the mass density,  $Z_i$  is the atomic number,  $A_i$  the atomic mass, and  $w_i$  the fraction by weight of the  $i$ th chemical element that composes the material  $m$ .

The reference stopping power values relative to water of the phantom inserts were computed using Bethe's equation without correction terms.<sup>2,11</sup> A 200 MeV initial kinetic energy was used and an ionization potential value of water of 78 eV was considered. Both the RED and the SPR reference values were computed with respect to G4-Water, i.e., water material from the Geant4 materials database, which slightly differs from Gammex Water material. Consequently, the reference SPR value of Gammex Water is 1.004 instead of 1 (see Fig. 1).

To make the study as realistic as possible, the irradiation geometry and the characteristics of a particular device, the imaging ring (IR) X-ray system (medPhoton, Salzburg, Austria), described by Rit et al.,<sup>24</sup> were employed in this study. The IR is a fast-kV switching system equipped with a filter wheel synchronized with the beam pulse. Nevertheless, the

results of this study could be extrapolated for any other dual-spectrum device. Virtual CT acquisitions of the IR were carried out by means of deterministic simulations in GATE<sup>25</sup> v7.2 using the fixed forced detection (FFD) actor. This deterministic module computes digitally reconstructed radiographs (DRR) using the reconstruction toolkit (RTK)<sup>26</sup> and the Geant4 database of X-ray cross sections. Only one slice was reconstructed using fan-beam projections with 360 views of 807 pixels of 1 mm without scatter were considered for the Gammex phantom, whereas 600 projections of 1026 pixels of 1 mm without scatter were considered for the ICRP phantom. The source-to-isocenter distance was 626 mm and the source-to-detector distance was 1026 mm. For the realistic scenario, Poisson noise was applied to the projections to deliver a central dose  $D_c$  with each spectrum while delivering a total central dose of 20 mGy with the dual-energy acquisition. The level of Poisson noise depends on the number of primary photons per simulation,  $N_{\text{prim}}$ , required to deliver a central dose of primary radiation,  $D_c$ , which was determined analytically assuming an homogeneous water medium:

$$N_{\text{prim}} = \frac{D_c A_{\text{beam}}}{\int_E S(E) e^{-\mu_w(E)} r \frac{\mu_{\text{en},w}(E)}{\rho_w} E dE} \quad (2)$$

where  $A_{\text{beam}}$  is the area covered by the beam at the isocenter considering a constant flat field,  $S$  is the energy-dependent incident spectrum with unity area:  $\int_E S(E) \cdot dE = 1$ ,  $\mu_{\text{en},w}(E)/\rho_w$  and  $\mu_w$  are respectively the energy-dependent mass energy-absorption coefficient and the linear attenuation coefficient of water taken from the NIST database,<sup>27</sup> and  $r$  is the radius of the phantom. The central dose  $D_c$  of 10 mGy per energy spectrum (20 mGy in total) was calculated at the center of a 33 cm diameter water phantom for the Gammex, the ICRP thorax slice, and the ICRP pelvis slice, whereas a 20 cm diameter water phantom was considered for the ICRP head slice. The energy-dependent detector response used in this study was previously validated by Vilches-Freixas et al.<sup>28</sup>

For each projection angle, a low-energy (LE) and a high-energy (HE) intensity value were obtained:

$$I_{\text{LE}} = \int_{E_{\text{min}}}^{E_{\text{max}}} S_{\text{LE}}(E) D(E) \exp\left(-\int_L \mu(\ell, E) d\ell\right) dE \quad (3)$$

$$I_{\text{HE}} = \int_{E_{\text{min}}}^{E_{\text{max}}} S_{\text{HE}}(E) D(E) \exp\left(-\int_L \mu(\ell, E) d\ell\right) dE \quad (4)$$

where  $L$  is the line segment between the source and a detector pixel,  $I_{\text{LE}}$  and  $I_{\text{HE}}$  are the measured intensities,  $S_{\text{LE}}$  and  $S_{\text{HE}}$  are the polychromatic photon spectra, and  $D(E)$  the detector response.

For each pair of X-ray spectra, the incident energy gap,  $\Delta E$ , was calculated as the separation between the average energies of the incident spectra:

$$\Delta E = \int_0^{E_2} S_{\text{HE}}(E) E dE - \int_0^{E_1} S_{\text{LE}}(E) E dE \quad (5)$$

where  $E_1$  and  $E_2$  are the maximum energies of the LE and the HE spectra, respectively.

## 2.B. Dual-energy spectra optimization

SpekCalc<sup>29–31</sup> was used to generate the X-ray spectra from 60 kV to 140 kV with 2 kV steps, 10° anode angle, 2.5 mm Al total filtration [required minimum filtration according to the NCRPM (1989)<sup>32</sup>], and 1000 mm air filtration. Each spectrum was filtered with pure tin (Sn), as suggested by Primak et al. (2009),<sup>20</sup> with thicknesses ranging from 0 to 2.5 mm in 0.1 mm increments. For the LE acquisitions, the tube voltage was varied from 60 kV to 100 kV, whereas for the HE acquisitions it was varied from 80 kV to 140 kV. No tin filtration was considered for the LE acquisitions to maximize the energy gap, only the 2.5 mm Al inherent filtration. In total, 16926 tuples (21 LE voltages, 31 HE voltages, and 26 Sn thicknesses) were evaluated.

In this spectra optimization study, the same dose at the center was considered for the low- and the high-energy acquisitions. In particular, a central dose  $D_c$  of 10 mGy with each voltage and filtration combination was used, and thus a total central dose of 20 mGy with the dual-energy acquisition.

For each (LE, HE, mm Sn) tuple, the reconstructed SPR image of the Gammex phantom was compared to the reference values (Fig. 1). The relative accuracy and precision were calculated in a circular region-of-interest (ROI) centered at the center of the insert with a radius of three-fourths the size of the insert (i.e., 10 pixels radius). The relative accuracy (RA) and precision (RP) of the SPR averaged over all inserts were computed as follows:

$$RA = \frac{1}{N} \sum_{m=1}^N \left( \frac{v_m^{\text{ref}} - \bar{v}_m}{v_m^{\text{ref}}} \right)^2 \quad (6)$$

$$RP = \sqrt{\frac{1}{N} \sum_{m=1}^N \left( \frac{\sigma_m}{v_m^{\text{ref}}} \right)^2} \quad (7)$$

where  $v_m^{\text{ref}}$ ,  $\bar{v}_m$ , and  $\sigma_m$  are respectively the reference SPR value (listed in Fig. 1), the mean SPR value inside the ROI and the standard deviation inside the ROI for the  $m^{\text{th}}$  insert, with  $N$  equal to 16.

## 2.C. Fractional dose allocation optimization

The same irradiation setup as described above was used to estimate the optimal dose balance between voltages that minimizes the uncertainty and the precision of the SPR. Table I shows the four dual-energy spectra selected for this study, with incident energy gaps comprised between 30 keV and 49 keV. The first pair of dual-energy spectra corresponds to the Siemens Flash spectra,<sup>33</sup> the second one to a possible pair of dual-energy spectra generated with the medPhoton Imaging Ring, whereas the others correspond, respectively, to the optimal dual-energy spectra for solid water and bone tissue obtained from the results of Section 2.B. The dose of the LE and the HE acquisitions are herein named  $D_{\text{LE}}$  and  $D_{\text{HE}}$ , respectively. For each pair of dual-energy spectra, the proportion of  $D_{\text{LE}}$  ( $D_{\text{HE}}$ ) with respect to the total dose was varied

TABLE I. Dual-energy spectra selected for the dose allocation study and the assessment of the proton range accuracy. From left to right: low-energy spectrum, high-energy spectrum with additional tin filtration and the corresponding energy gap.

#	LE spectrum	HE spectrum	$\Delta E$ (keV)	Description
1	80 kVp	140 kVp + 0.4 mm Sn	43	Siemens Flash spectra
2	60 kVp	120 kVp + 0.6 mm Sn	48	medPhoton Imaging Ring spectra
3	90 kVp	110 kVp + 0.5 mm Sn	30	Solid water optimal DE spectra
4	80 kVp	106 kVp + 2.2 mm Sn	49	Bone tissue optimal DE spectra

from 10% (90%) to 90% (10%) by steps of 20% while keeping the phantom dose at the center to a constant value of 20 mGy. For each dose level, the corresponding Poisson noise was computed using Eq. (2) and it was applied to the projections through the FFD actor of GATE. In total, considering the four pairs of dual-energy spectra and the five dose levels evaluated per spectra, 20 noise levels were computed with Eq. (2). For each noise level, i.e., for each pair of dual-energy spectra and dose proportion, 25 realizations of noise in the projection images were generated to estimate the accuracy and the precision. Then, the SPR value inside a 10 pixels radius ROI inside each insert was computed for each set and compared to the reference values. The overall accuracy and precision of the SPR averaged over all inserts were also computed [Eqs. (6) and (7)].

## 2.D. SPR determination

The proposed method to compute the SPR from dual-energy data in the projection domain is an adaptation of the two-steps procedure proposed by Farace<sup>34</sup> in the image domain. It consists of two steps: first, determination of the RED image through the two-material decomposition method proposed by Alvarez and Macovski<sup>5</sup> implemented in the projection domain; and second, determination of the SPR image using the poly-lines relations proposed by Kanematsu et al.<sup>12</sup>

The key idea of the two-materials method is that the linear attenuation coefficient of the scanned object at any spatial position  $x$  and energy  $E$ ,  $\mu(x, E)$ , can be expressed as a linear combination of two energy-dependent basis functions of two materials with energy-independent coefficients. Choosing water (w) and compact bone (b) as basis materials, it is assumed that

$$\mu(x, E) = \rho_w(x) \left( \frac{\mu}{\rho} \right)_w (E) + \rho_b(x) \left( \frac{\mu}{\rho} \right)_b (E) \quad (8)$$

where  $\mu/\rho$  denotes the energy-dependent mass attenuation coefficients and  $\rho$  the mass fraction per volume.

By performing an acquisition with LE and HE spectra, two sinograms of the same object are available. For every angle  $\theta$  and pixel location  $u$ , we have

$$\hat{I}_{\text{LE}}(\theta, \mathbf{u}) = -\ln \left[ \frac{I_{\text{LE}}(\theta, \mathbf{u})}{I_{\text{LE}}^0(\theta, \mathbf{u})} \right] \quad (9)$$

$$\hat{I}_{\text{HE}}(\theta, \mathbf{u}) = -\ln \left[ \frac{I_{\text{HE}}(\theta, \mathbf{u})}{I_{\text{HE}}^0(\theta, \mathbf{u})} \right] \quad (10)$$

where  $I_{\text{LE}}$  and  $I_{\text{HE}}$  are the intensities measured in the presence of the object, while  $I_{\text{LE}}^0$  and  $I_{\text{HE}}^0$  are the intensities measured in the absence of the object. The projection of the mass densities are given by

$$a_w(\theta, \mathbf{u}) = \int_{L(\theta, \mathbf{u})} \rho_w(\ell) d\ell \quad (11)$$

$$a_b(\theta, \mathbf{u}) = \int_{L(\theta, \mathbf{u})} \rho_b(\ell) d\ell \quad (12)$$

where  $L(\theta, \mathbf{u})$  is the line segment between the source and a detector pixel located at position  $\mathbf{u}$  for the view angle  $\theta$ . The projected mass densities  $\{a_w, a_b\}$  can be expressed as a polynomial function of the logarithmic transmission values  $\{\hat{I}_{\text{LE}}, \hat{I}_{\text{HE}}\}$ <sup>36,35</sup> at every angle  $\theta$  and pixel location  $\mathbf{u}$ , i.e.,

$$a_w = \mathcal{P}_w(\hat{I}_{\text{LE}}, \hat{I}_{\text{HE}}) \quad (13)$$

$$a_b = \mathcal{P}_b(\hat{I}_{\text{LE}}, \hat{I}_{\text{HE}}) \quad (14)$$

The coefficients of the polynomial  $\mathcal{P}_w$  and  $\mathcal{P}_b$  can be obtained through a calibration procedure in the least squares sense. Attenuation measurements were performed for two different photon spectra (labeled LE and HE) interposing slabs of two well-known materials with variable thicknesses. It is important that the calibration phantom covers all possible path length variations through each basis material, and combinations of path lengths through both materials.<sup>37</sup> In this study, water thicknesses ranging from 0 to 38 cm with 1 mm steps and compact bone thicknesses comprised between 0 and 15 cm in 1 mm increments were used for the calibration. A fourth degree polynomial with 15 terms was initially considered. A stability study to noise, similar to that conducted by Létang et al.,<sup>38</sup> was performed to determine which terms of the polynomial were more unstable and, thus, eliminated. Finally, a fourth degree polynomial with 12 terms was found to be adequate to solve this system of equations.

Then, image reconstruction of water and compact bone mass densities were performed using the filtered backprojection (FBP) reconstruction of RTK on a  $380 \times 380$  pixel grid with  $1 \times 1 \text{ mm}^2$  pixels size for the Gammex images, and on a  $299 \times 137$  pixel grid with  $1.775 \times 1.775 \text{ mm}^2$  pixels size for the ICRP images.

Finally, on a pixel-by-pixel basis, the RED image was derived from the reconstructed mass density images,  $\rho_w(\mathbf{x})$  and  $\rho_b(\mathbf{x})$ , the number of electrons per molecular weight of each basis material and the tabulated electron density of water (i.e., G4-water for consistency with reference RED and SPR values),  $\rho_{e,w}$ , divided by the Avogadro's number,  $N_A$ :

$$\text{RED}(\mathbf{x}) = \frac{\rho_w(\mathbf{x}) \left[ \sum_i w_i \frac{Z_i}{A_i} \right]_w + \rho_b(\mathbf{x}) \left[ \sum_i w_i \frac{Z_i}{A_i} \right]_b}{\left( \frac{\rho_{e,w}}{N_A} \right)} \quad (15)$$

The reconstructed RED values were directly converted into SPR through the piecewise linear relations of the RED and the ratio between SPR and RED of human tissues as suggested by Kanematsu.<sup>12</sup> To reproduce Fig. 1(a) of Kanematsu et al.,<sup>12</sup> a selection of 92 ICRU 46<sup>39</sup> body tissues, excluding obsolete or artificially extracted materials, were used to perform the calibration. The SPR values of these body tissues were calculated using Bethe's equation without correction terms at 200 MeV, as done for the Gammex and the ICRP SPR reference values.

## 2.E. Proton range prediction

To estimate the accuracy of the proton range prediction, three slices of the ICRP phantom were selected: head, thorax, and pelvis. Three proton energies were considered: 70 MeV (head), 90 MeV (thorax), and 100 MeV (pelvis). The corresponding ranges in water  $R_{\text{water}}$ , according to the continuous slowing down approximation,<sup>40</sup> were 40.8 mm, 64.0 mm, and 77.2 mm, respectively. These beam energies have no clinical relevance, they have been chosen to avoid irradiating twice the same phantom area with coplanar beams. The proton range in the phantom computed at each angle  $\theta$ , where  $\theta$  ranges from 0 to  $360^\circ$  in  $5^\circ$  step around the center of the phantom, was determined as the phantom depth  $R_\theta$  where the water equivalent thickness, defined as the integral of the phantom SPR along the proton beam path, matched the proton range in water:

$$R_{\text{water}} = \int_0^{R_\theta} \text{SPR}_\theta(l) dl \quad (16)$$

where  $\text{SPR}_\theta$  is the 1D profile of the SPR image along the proton beam path for the incident angle  $\theta$ . The SPR was computed for the dual-energy spectra shown in Table I. To quantify the gain with respect to single-energy imaging, scanner simulations of the Gammex phantom performed at 120 kVp filtered with 0.2 mm Sn were used to generate a CT number to SPR calibration curve (Fig. 3). A CT acquisition of the AF ICRP phantom at 120 kVp/Sn was used to derive the corresponding SPR map through this SECT calibration curve. Both for single-energy and dual-energy, two dose levels were considered: SPR images computed without imaging noise (infinite dose or ideal case) and SPR images computed with a 20 mGy central dose. For the latter, for each anatomical region and spectra, the range was assessed on 25 SPR images reconstructed from different noise realizations.

The proton range estimated from DECT and SECT SPR maps were compared to the range calculated from the reference SPR map (Fig. 2).

For each imaging situation and noise setup, the histogram of the proton range differences over all irradiation angles was

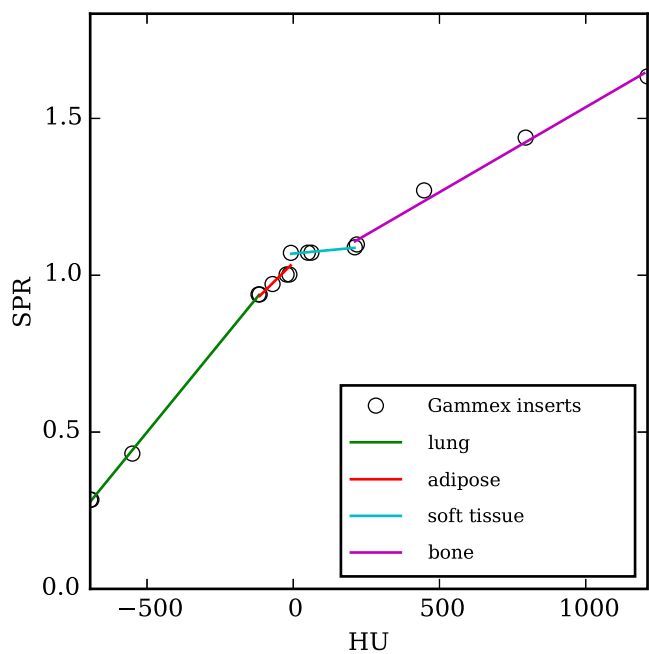


FIG. 3. HU to SPR calibration curve for SECT scanner simulations of the Gammex phantom at 120 kVp/Sn. A piece-wise linear interpolation between HU and SPR values was used, divided in four segments: lung tissue, adipose tissue, soft tissue, and bone tissue. [Color figure can be viewed at [wileyonlinelibrary.com](#)]

fitted with a Gaussian distribution ( $\mu \pm \sigma$ ). In addition, the RMS error and the maximum error were also computed.

### 3. RESULTS

#### 3.A. Dual-energy spectra optimization

In this spectra optimization study, a total of 16926 tuples were considered by combining 21 LE voltages, 31 HE voltages, and 26 Sn-thicknesses. For the realistic scenario

(images with a 20 mGy central dose and equal dose weight per energy channel), the overall SPR accuracy and precision were plotted against the incident energy gap (Fig. 4). The overall accuracy [Eq. (6)] was not strongly dependent on the spectra separation, with a minimum in the 25–35 keV range of energy gaps where the maximum separation is about 80 keV. In addition, dual-energy spectra combinations with an energy gap above 30 keV resulted in an overall accuracy within  $\pm 0.6\%$ . The overall precision [Eq. (7)] asymptotically approached a 4.7% level with increasing energy gap. This level of precision was achieved for energy gaps larger than 60 keV.

A zero precision was expected for the simulations without noise. However, images reconstructed from noiseless discrete projections always display residual noise caused by discrete filtering and image interpolation during backprojection. A constant value of 2.6% was observed for all SPR images without noise. In other words, the horizontal line in Fig. 4(b) would be shifted to 2.6% in the case of noiseless simulations. This residual noise level is also present in the noisy simulations of Fig. 4 but combined with the photon noise.

To understand why the energy gap is not a good metric to determine the dual-energy spectra that minimizes the overall SPR accuracy, one representative insert per tissue group was selected: LN-300(8) for the low ( $RED < 0.5$ ), Solid Water(7) for the medium ( $0.5 < RED < 1.2$ ), and CB2-50(1) for the high ( $RED > 1.2$ ) density. One optimal dual-energy spectra per tissue group was determined looking at the accuracy inside the corresponding ROI for all spectra combinations. Around this (LE, HE, Sn) tuple, orthogonal slices were plotted to study the dependence of the insert accuracy with the low voltage, the high voltage, and the additional filtration. The plots relative to the ideal situation are shown in Fig. 5. Different optimal points were found for different tissue types, which suggests tissue variability with respect to the optimal energy spectra.

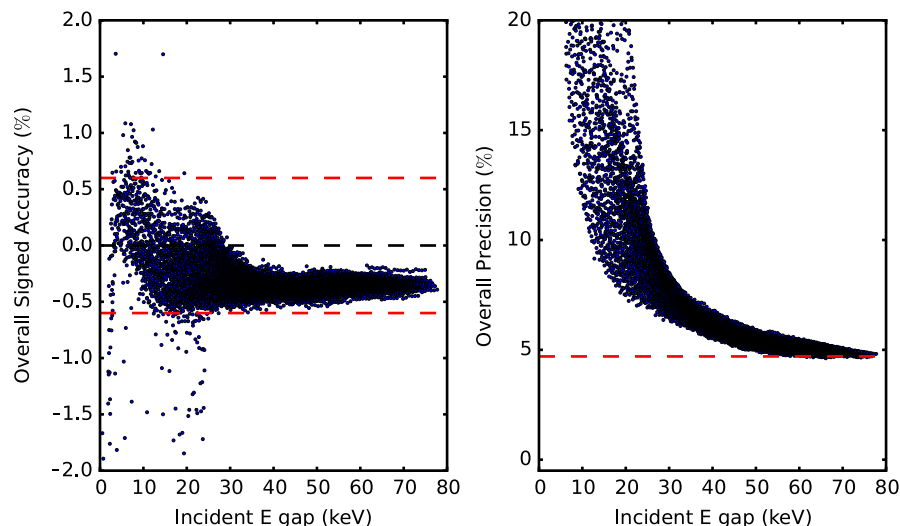


FIG. 4. Overall SPR accuracy and precision as a function of the incident energy gap for the realistic acquisition scenario (20 mGy central dose) and the same dose weight per voltage. Each of the 16926 data points corresponds to a (LE, HE, mm Sn) combination. Horizontal dashed red lines indicate the  $\pm 0.6\%$  accuracy level (left) and the 4.7% precision level (right). [Color figure can be viewed at [wileyonlinelibrary.com](#)]

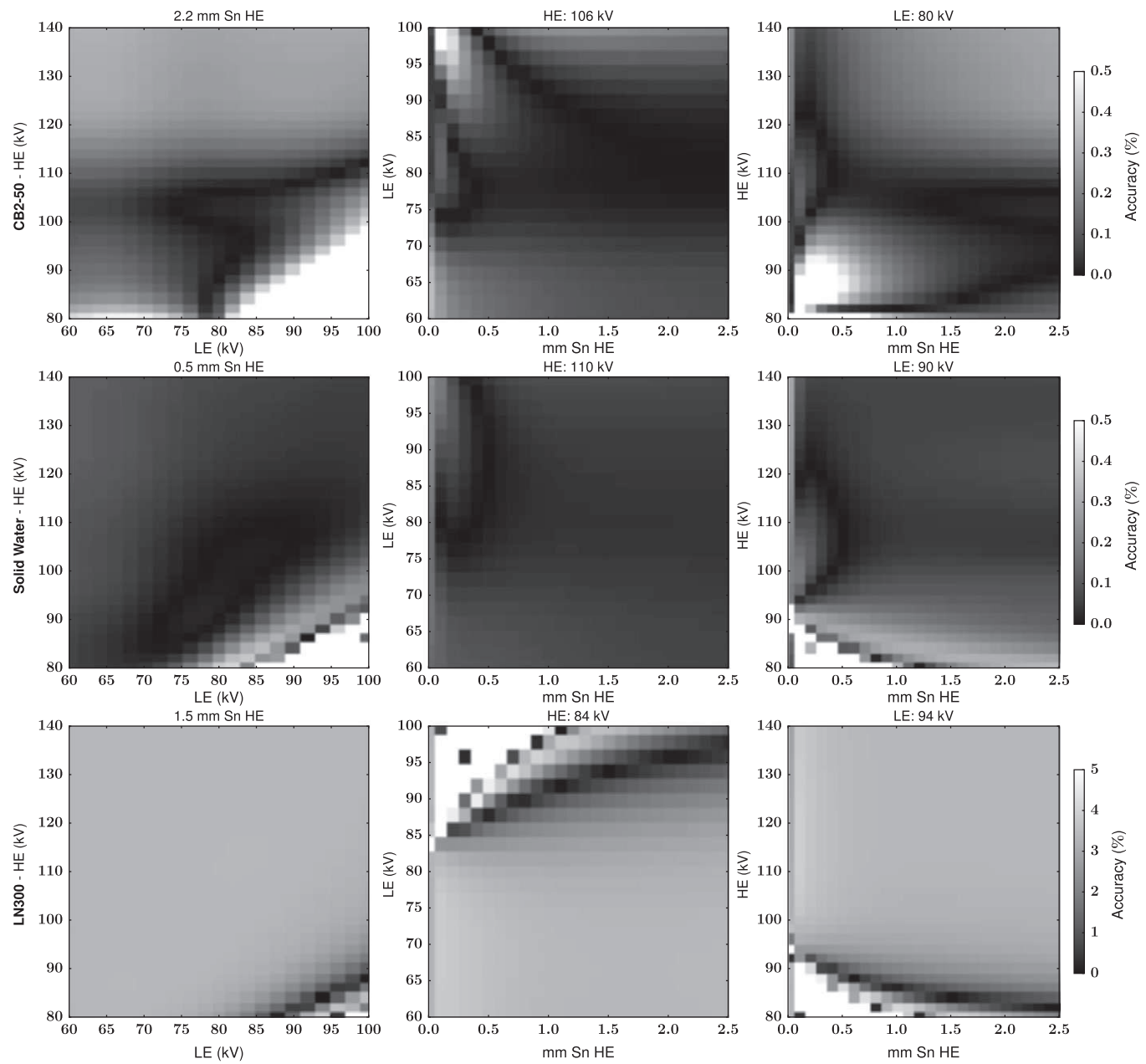


Fig. 5. From top to bottom, SPR accuracy results as a function of the LE, HE, and tin filtration for the insert: CB2-50, Solid Water, and LN-300. From left to right: LE-HE plot at the optimal Sn thickness, LE-mm Sn plot at the optimal HE, HE-mm Sn plot at the optimal LE. The grayscale indicates the percentage error for the accuracy in absolute value. Note the different scale for the CB2-50 and the Solid Water with respect to the LN-300 insert. Data corresponding to the ideal situation, without noise.

To investigate why there are some energy windows that produce better accuracy results than others, the ratio between the theoretical linear attenuation coefficient (retrieved from NIST<sup>27</sup>) and the estimated value [obtained through Eq. (8)] as a function of the monochromatic energy was computed for the same Gammex inserts as in Fig. 5: CB2-50, Solid Water, and LN-300. For each insert, two dual-energy spectra were considered: one that maximizes the SPR accuracy and one that does not provide a good accuracy. Plot of the ratio between theoretical and estimated  $\mu$  values for the three Gammex inserts is shown in Fig. 6. The  $\mu$  ratio being close to one for the entire range of the dual-energy spectra seems to

correlate well with better SPR accuracy results. Solid water seems to be less dependent on the dual-energy spectra, as also shown in Fig. 5, where most of the spectra provide a good level of accuracy. On the other hand, bone tissue and lung tissue present well-defined energy windows where the level of accuracy is optimal and areas where it is not.

### 3.B. Fractional dose allocation optimization

The impact of the dose balance between the low- and the high-energy projections was studied using 25 SPR images for each pair of dual-energy spectra of Table I and dose ratio

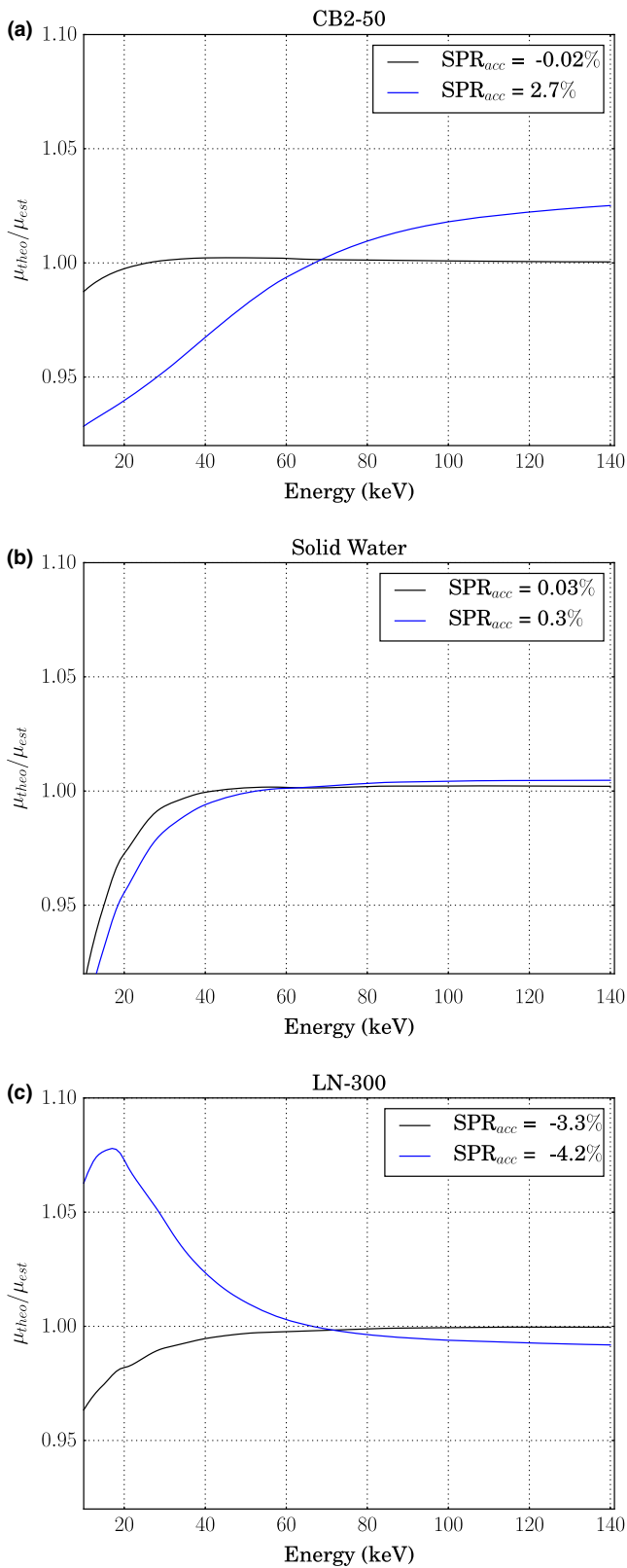


FIG. 6. Ratio between the theoretical  $\mu$  and the estimated  $\mu$  value derived from Eq. (8) as a function of the energy for three Gammex inserts. From top to bottom: CB2-50 (a), Solid Water (b), and LN-300 (c). Legend shows the SPR accuracy corresponding to one optimal dual-energy spectra (black) and to one sub optimal dual-energy spectra (blue). [Color figure can be viewed at [wileyonlinelibrary.com](http://wileyonlinelibrary.com)]

(i.e., from 10% to 90%), obtained after decomposition and reconstruction of different noise realizations.

The boxplots of the overall precision [Eq. (7)] and accuracy [Eq. (6)] as a function of the dose distribution between the LE and the HE acquisitions are shown in Fig. 7. The overall precision presented a minimum around 30% D<sub>LE</sub> (70% D<sub>HE</sub>) for all spectra. As shown in Fig. 4, Fig. 7 confirms that the precision improves when the energy separation between the incident energy spectra increases. In terms of accuracy, the overall accuracy is almost flat in the range 30–70% D<sub>LE</sub> (70–30% D<sub>HE</sub>). Around 90% D<sub>LE</sub> (10% D<sub>HE</sub>) the overall accuracy seems to be improved (Fig. 7, bottom). However, the precision is two times larger than the 70% D<sub>LE</sub> (30% D<sub>HE</sub>) proportion (Fig. 7, top) and noise therefore masks the validity of the accuracy at this point.

### 3.C. Proton range prediction

Proton beam irradiations were simulated from 360 directions in 5° step around the center of the ICRP phantom slices. The proton ranges for 70 MeV, 90 MeV, and 100 MeV were

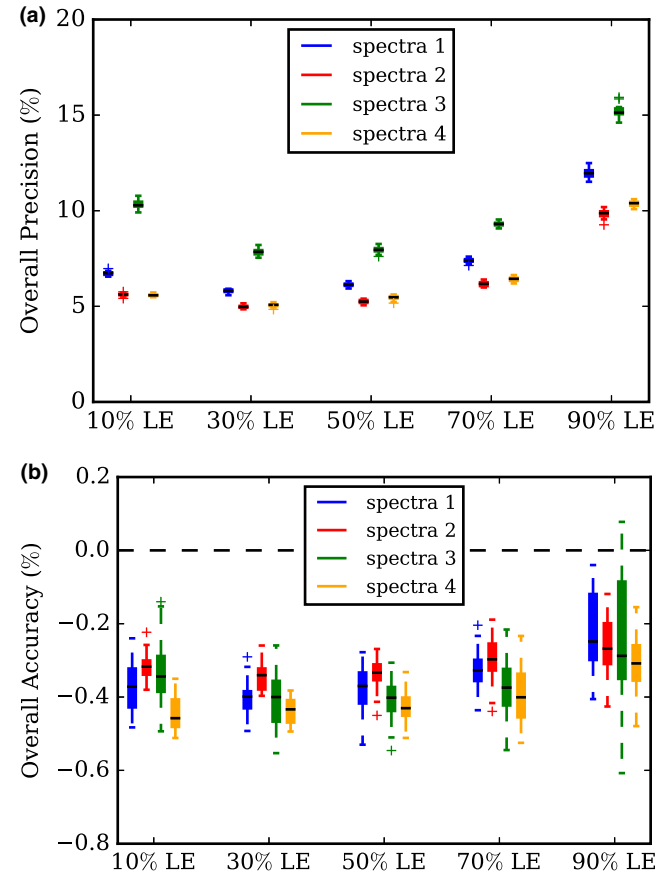


FIG. 7. Overall precision (a) expressed in terms of the root-mean-squared (RMS) error, and overall accuracy (b) determined as the mean signed deviation, averaged over all inserts, as a function of the dose allocation between the LE and the HE acquisitions. The dual-energy spectra are described in Table I. [Color figure can be viewed at [wileyonlinelibrary.com](http://wileyonlinelibrary.com)]

TABLE II. Signed mean errors ( $\mu \pm \sigma$ ), maximum deviations on the proton range estimation (max) and root-mean square (RMS) errors over 360 directions at 5° steps for the ideal situation (without noise) and the realistic scenario (at 20 mGy).

Spectra	Without noise			20 mGy		
	$\mu \pm \sigma$ (mm)	max (mm)	RMS (mm)	$\mu \pm \sigma$ (mm)	max (mm)	RMS (mm)
Head						
1	-0.04 ± 0.50	1.9	0.51	-0.05 ± 0.55	2.1	0.55
2	-0.13 ± 0.55	1.9	0.56	-0.12 ± 0.56	2.1	0.57
3	0.07 ± 0.49	1.9	0.50	0.07 ± 0.51	2.0	0.51
4	-0.04 ± 0.51	1.9	0.51	-0.05 ± 0.53	2.1	0.54
SECT	0.46 ± 0.67	1.9	0.81	0.47 ± 0.67	2.0	0.82
Thorax						
1	-0.10 ± 0.70	2.7	0.71	-0.10 ± 0.73	3.8	0.74
2	-0.14 ± 0.71	2.8	0.72	-0.15 ± 0.76	3.7	0.77
3	0.00 ± 0.69	2.5	0.69	-0.00 ± 0.77	3.8	0.76
4	-0.13 ± 0.68	2.6	0.69	-0.09 ± 0.74	3.8	0.75
SECT	0.28 ± 0.81	3.2	0.86	0.29 ± 0.82	3.5	0.87
Pelvis						
1	-0.15 ± 0.52	1.9	0.55	-0.23 ± 0.64	3.0	0.70
2	-0.18 ± 0.56	1.8	0.59	-0.24 ± 0.61	2.0	0.66
3	-0.13 ± 0.50	1.9	0.51	-0.20 ± 0.71	2.9	0.74
4	-0.15 ± 0.52	1.8	0.55	-0.23 ± 0.61	2.0	0.65
SECT	0.09 ± 0.58	1.8	0.59	0.11 ± 0.64	2.0	0.65

computed from the DECT-derived SPR images, the SECT-derived SPR images and from the reference SPR maps.

Signed mean errors, maximum deviations, and RMS errors on the proton range estimation over 360 directions at 70 MeV (head), 90 MeV (thorax), and 100 MeV (pelvis) are shown in Table II for the ideal situation (without noise) and the realistic scenario (at a central dose of 20 mGy).

#### 4. DISCUSSION

This simulations-based study comparing many pairs of dual-energy spectra demonstrates that the energy separation between the incident spectra had a strong influence on the SPR precision. It was observed that above an energy gap of 60 keV, the precision asymptotically tends to a 4.7% level. This result is in agreement with Primak et al. (2009),<sup>20</sup> in which they established a relation between the dual-energy ratio of two materials and the image quality. They found that a small difference between the dual-energy spectra resulted in a significant increase of the noise. To improve image quality, they optimized the additional filtration to increase the energy gap.

Our study indicates that the energy gap is not a good metric to determine the optimal spectra when looking at the SPR accuracy averaged over all tissues. The reason is that a large variability of the optimal spectra was observed when studying each phantom material separately (Fig. 5). Therefore, the optimization of the dual-energy spectra must be based on the materials present in the anatomical region traversed by

the proton beams. This result confirms that the optimal spectra in dual-energy imaging is task-,<sup>41</sup> site-, and patient-dependent.

The choice of the material basis (water and compact bone), the choice of the order of the polynomial, the presence of crossed terms in the polynomial, and the choice of the dual-energy spectra are factors that determine the correctness of Eq. (8), which is the main hypothesis of the employed decomposition method. In addition, to obtain acceptable results in terms of accuracy, the validity of Eq. (8) has to be verified within the spectral energy range of the incident spectra (Fig. 6).

With respect to the dose allocation study, it was found that the dose balance between energy levels was not critical for the SPR estimation. In fact, the overall accuracy was almost flat in the 30–70% D<sub>LE</sub> range (Fig. 7, right). This result agrees with a previous study<sup>42</sup> conducted for an image-based decomposition method and a different figure of merit: the accuracy on the extracted Z<sub>eff</sub>. A plausible explanation is that even if the high-energy spectrum is more penetrating than the low-energy spectrum, this effect is compensated with the poorer efficiency of the detector response at high energy (Fig. 1 of Vilches-Freixas et al.<sup>28</sup>). On the other hand, the precision presents a minimum slightly shifted in favor of lower dose for the lower voltage spectrum (i.e., 30% LE-dose). Shkumat et al. (2007)<sup>18</sup> came to the same conclusion; the optimal image quality, in terms of SNR, was achieved when one-third of the total dose was imparted with the LE acquisition.

Two scenarios were evaluated to determine the accuracy of the proton range prediction: an ideal case with an infinite dose, i.e., X-ray simulations without noise, and a realistic situation with a 20 mGy central dose. The SPR images of the ICRP phantom were reconstructed using four representative dual-energy spectra (see Table I). The differences between the four pairs of spectra in Table II were small ( $|\mu| < 0.2$  mm) and not significant (two-tailed paired t-test,  $P > 0.1$ ) due to the variability between beams ( $\sigma > 0.49$  mm). In practice, precision could therefore drive the choice of spectra, i.e., the energy gap (Fig. 4, right). When comparing DECT range errors with SECT range errors, all dual-energy spectra provided a range improvement for the head and for the thorax slices. Although this was not the case for the pelvis slice, this confirms the limitations of SECT, with variations from site-to-site and the results would have been different if another calibration curve had been used than the one in Fig. 3, as observed by Arbor et al.<sup>43</sup> All pairs of DECT spectra seemed robust on average over all sites. Based on these results, the gain in SPR accuracy obtained when optimizing the dual-energy spectra based on the materials traversed by the proton path is not translated into improved proton range estimation, as comparable range differences were obtained with the four dual-energy spectra.

For radiotherapy applications, based on the ALARA principle (As Low As Reasonably Achievable), a trade-off between dose and image noise should be found. From one side, an imaging dose lower than 20 mGy might not result appropriate as it would trigger excessive image noise. From the other side, increasing the dose or implementing a regularized reconstruction algorithm instead of using filtered-back-

projection could be valid alternatives to reduce image noise. Signed mean errors and RMS errors for the realistic scenario were found to be comparable to those of the noiseless situation (infinite dose), specially for the head and the thorax slices, despite a rather small increase in the maximum error values (see Table II). For the pelvis slice a higher impact of noise on the range results was observed. Nevertheless, according to these results, the presence of noise in the SPR image seems to have a rather low impact on the range estimation as noise is averaged along the voxels of the beam path.

Uncertainties in the beam direction, such as changes in density and tissue inhomogeneities caused by movement, patient misalignment or anatomical changes, or uncertainties in determining the SPR of tissues, have a severe impact on the proton range and can cause severe damages to the patient, such as target miss or accidental exposure of organs-at-risk. Benefits of using dual-energy imaging for treatment planning to improve the estimation of the SPR of tissues, as an alternative to single-energy CT calibration, assuming a nonmoving target have been evaluated in this work. However, it should be noted that a 3.5% range uncertainty is commonly associated to the single-energy calibration curve between CT numbers and SPR values using a real CT scanner system but range errors obtained in Table II are much lower than 3.5%. The reason is that in this simulation-based study, we only focused on the range uncertainty associated to the conversion of CT numbers into SPR values. We have considered an idealized irradiation setup, neglecting real CT scanner issues such as X-ray scatter, motion artifacts, and time stability. Moreover, besides the uncertainties in the longitudinal direction, other sources of uncertainty exist in proton therapy such as density changes perpendicular to the beam direction, the effect of lateral beam penumbra, or incorrect proton scatter modeling in analytical treatment planning systems,<sup>1</sup> which might have a severe dosimetric impact in proton therapy dose calculations.

In this work, we propose a full projection-based decomposition method framework for the treatment planning of proton therapy. Despite the fact that no consensus has been reached within the community to prefer one method over the others, nor a decomposition domain (projection — or image — domain) for the SPR estimation, projection-based methods present the advantage to be intrinsically less affected by beam-hardening than image-based approaches. One assumption of projection-based methods is that the same information per tube voltage is available at each projection angle. This prerequisite can be seen as a disadvantage when using dual-source scanners as independent rotations around the patient are performed, however, with the advent of technological developments, this requirement can be fulfilled by using dual-layer detectors or photon counting detectors systems, for which it is possible to acquire low and high energy projections at the same angle. Fast-kV switching imaging systems equipped with a synchronized filter wheel, such as the Imaging Ring, approach this requirement on the condition that interpolation of consecutive projections is performed. Besides, the proposed method to estimate the SPR images from dual-energy data in the projection-domain is an

adaptation of the two-steps procedure proposed by Farace et al. in the image-domain,<sup>34</sup> which produced comparable results with respect to Hünemohr's approach.<sup>9</sup>

One limitation of this study is that the investigated acquisition parameters (i.e., spectral separation and dose allocation) are only meaningful for dual-spectrum scanners but not for dual-detector systems. In addition, we have used a projection-based decomposition algorithm to evaluate the acquisition parameters and it would be interesting to repeat the same study using an image-based decomposition algorithm. However, image-based methods require the implementation of a beam-hardening correction for each X-ray spectrum.

For each dual-energy spectra evaluated, a virtual image-simulation calibration curve, interposing slabs of two materials of known thickness and composition, was performed to solve the system of Eqs. (3) and (4). In this case, the dual-energy spectra were an input of this virtual simulation and we assumed that the spectra were perfectly known. A realistic detector response model has been used and a Poisson noise proportional to a certain dose value has been applied to the projections, but we have neglected scattered photons. We might expect a significant effect of scatter on the material decomposition, and scatter-compensation techniques prior to the decomposition should be implemented for large X-ray beams,<sup>44</sup> such as cone-beam irradiations.

## 5. CONCLUSION

This study evaluated the impact of the dual-energy spectra and the dose allocation between energy levels on the proton stopping power ratio accuracy and precision based on a projection-based dual-energy decomposition approach, which can guide the choice of spectra for dual-energy CT for proton therapy. The effect of the SPR accuracy and precision on the proton range estimation was also investigated. An ideal situation without noise and a realistic acquisition with a total central dose of 20 mGy were considered. The precision was improved increasing the energy separation between the incident spectra, whereas the accuracy showed little dependence to the energy gap. The dose balance between energy levels was not found to be sensitive for the SPR estimation. The optimal pair of dual-energy spectra was material dependent but on a heterogeneous anthropomorphic phantom, there was no significant difference in range accuracy and the choice of spectra could be driven by the precision, i.e., the energy gap.

## ACKNOWLEDGMENTS

This work was partially supported by grant ANR-13-IS03-0002-01 (DEXTER project) from the French National Research Agency (ANR). This work was performed within the framework of the LABEX PRIMES (ANR-11-LABX-0063) of Université de Lyon, within the program "Investissements d'Avenir" (ANR-11-IDEX-0007) operated by the ANR. We also gratefully acknowledge the support from the CNRS/IN2P3 Computing Center (Lyon/Villeurbanne France) for providing a significant amount of the computing

resources needed for this work. The authors have no relevant conflicts of interest to disclose.

<sup>a)</sup>Author to whom correspondence should be addressed. Electronic mail: simon.rit@creatis.insa-lyon.fr.

## REFERENCES

- Paganetti H. Range uncertainties in proton therapy and the role of Monte Carlo simulations. *Phys Med Biol.* 2012;57:R99–R117.
- Schneider U, Pedroni E, Lomax A. The calibration of CT Hounsfield units for radiotherapy treatment planning. *Phys Med Biol.* 1996;41:111–124.
- Yang M, Zhu XR, Park PC, et al. Comprehensive analysis of proton range uncertainties related to patient stopping-power-ratio estimation using the stoichiometric calibration. *Phys Med Biol.* 2012;57:4095–4115.
- Van Elmpt W, Landry G, Das M, Verhaegen F. Dual energy CT in radiotherapy: current applications and future outlook. *Radiat Oncol.* 2016;119:137–144.
- Alvarez RE, Macovski A. Energy-selective reconstructions in X-ray computerized tomography. *Phys Med Biol.* 1976;21:733–744.
- Tremblay J-É, Bedwani S, Bouchard H. A theoretical comparison of tissue parameter extraction methods for dual energy computed tomography. *Med Phys.* 2014;41:081905.
- Bazalova M, Carrier J-F, Beaulieu L, Verhaegen F. Tissue segmentation in Monte Carlo treatment planning: a simulation study using dual-energy CT images. *Radiat Oncol.* 2008;86:93–98.
- Landry G, Seco J, Gaudreault M, Verhaegen F. Deriving effective atomic numbers from DECT based on a parameterization of the ratio of high and low linear attenuation coefficients. *Phys Med Biol.* 2013;58:6851–6866.
- Hünemohr N, Krauss B, Tremmel C, Ackermann B, Jäkel O, Greilich S. Experimental verification of ion stopping power prediction from dual energy CT data in tissue surrogates. *Phys Med Biol.* 2014;59:83–96.
- Bourque AE, Carrier J-F, Bouchard H. A stoichiometric calibration method for dual energy computed tomography. *Phys Med Biol.* 2014;59:2059–2088.
- Yang M, Virshup G, Clayton J, Zhu XR, Mohan R, Dong L. Theoretical variance analysis of single- and dual-energy computed tomography methods for calculating proton stopping power ratios of biological tissues. *Phys Med Biol.* 2010;55:1343–1362.
- Kanematsu N, Inaniwa T, Koba Y. Relationship between electron density and effective densities of body tissues for stopping, scattering, nuclear interactions of proton and ion beams. *Med Phys.* 2012;39:1016–1020.
- Möhler C, Wohlfahrt P, Richter C, Greilich S. Range prediction for tissue mixtures based CT on dual-energy. *Phys Med Biol.* 2016;61:N268–N275.
- Vilches-Freixas G, Létang J-M, Rit S. Comparison of stopping-power estimators from dual-energy computed tomography for proton therapy. In ESTRO35; 2016. pp. EP-1276.
- Henzler T, Fink C, Schoenberg SO, Schoepf UJ. Dual-energy CT: radiation dose aspects. *AJR Am J Roentgenol.* 2012;199:16–25.
- Xu T, Ducote JL, Wong JT, Molloj S. Feasibility of real time dual-energy imaging based on a at panel detector for coronary artery calcium quantification. *Med Phys.* 2006;33:1612–1622.
- Saito M. Dual-energy approach to contrast-enhanced mammography using the balanced filter method: spectral optimization and preliminary phantom measurement. *Med Phys.* 2007;34:4236–4246.
- Shkumat NA, Siewersden JH, Dhanantwari AC, et al. Optimization of image acquisition techniques imaging for dual-energy. *Med Phys.* 2007;10:3904–3915.
- Granton PV, Pollmann SI, Ford NL, Drangova M, Holdsworth DW. Implementation of dual- and triple-energy cone-beam micro-CT for postreconstruction material decomposition. *Med Phys.* 2008;35:5030–5042.
- Primak AN, Ramirez Giraldo JC, Liu X, Yu L, McCollough CH. Improved dual-energy material discrimination for dual-source CT by means of additional spectral filtration. *Med Phys.* 2009;36:1359–1369.
- Rigie DS, La Rivière PJ. Optimizing spectral CT parameters for material classification tasks. *Phys Med Biol.* 2016;61:4599–4623.
- ICRP. Adult Reference Computational Phantoms. *Ann. ICRP.* 2009;39:3–5. ICRP Publication 110.
- Kanematsu N, Inaniwa T, Nakao M. Modeling of body tissues for Monte Carlo. *Phys Med Biol.* 2004;14:2016.
- Rit S, Clackdoyle R, Keuschning P, Steininger P. Filtered-backprojection reconstruction for a cone-beam computed tomography scanner with independent source and detector rotations. *Med Phys.* 2016;43:2344–2352.
- Jan S, Santin G, Strul D, Staelens S, Assié K, Autret D. GATE : a simulation toolkit for PET and SPECT. *Phys Med Biol.* 2004;49:4543–4561.
- Rit S, Vila Oliva M, Brousseau S, Labarbe R, Sarrut D, Sharp GC. The reconstruction toolkit (RTK), an open-source cone-beam CT reconstruction toolkit based on the insight toolkit (ITK) *J Phys Conf Ser.* 2014;489:012079.
- Hubbel JH, Seltzer SM. *Tables of X-ray Mass Attenuation Coefficients and Coefficients Mass Energy-Absorption* (version 1.4). Gaithersburg, MD: National Institute of Standards and Technology; 2004. <https://www.nist.gov/pml/x-ray-mass-attenuation-coefficients>.
- Vilches-Freixas G, Létang JM, Brousseau S, et al. Technical note : procedure for the calibration and validation of kilo-voltage cone-beam CT models. *Med Phys.* 2016;43:5199–5204.
- Poludniowski GG. Calculation of x-ray spectra emerging from an x-ray tube. Part II. X-ray production and filtration in x-ray targets. *Med Phys.* 2007;34:2175–2186.
- Poludniowski GG, Evans PM. Calculation of x-ray spectra emerging from an x-ray tube. Part I. electron penetration characteristics in x-ray targets. *Med Phys.* 2007;34:2164–2174.
- Poludniowski G, Landry G, DeBlois F, Evans PM, Verhaegen F. SpekCalc: a program to calculate photon spectra from tungsten anode x-ray tubes. *Phys Med Biol.* 2009;54:N433–N438.
- NCRPM. National Council on Radiation Protection and Measurements Medical x-ray, electron beam and gamma-ray protection from energies up to 50 MeV, Report No. 102. Report No.102. Bethesda, M.; 1989.
- Primak AN, Ramirez Giraldo JC, Eusemann CD, et al. Dual-source dual-energy CT with additional tin filtration: dose and image quality evaluation in phantoms and in-vivo. *AJR Am J Roentgenol.* 2010;195:1164–1174.
- Farace P. Comment: experimental verification of ion stopping power prediction from dual energy CT data in tissue surrogates. *Phys Med Biol.* 2014;59:7081–7084.
- Chuang K-S, Huang HK. Comparison of four dual energy image decomposition methods. *Phys Med Biol.* 1988;33:455.
- Lehmann L-A, Alvarez RE, Macovski A, et al. Generalized image combinations in dual KVP digital radiography. *Med Phys.* 1981;8:659–667.
- Stenner P, Berkus T, Kachelrieß M. Empirical dual energy calibration (EDEC) for cone-beam computed tomography. *Med Phys.* 2007;34:3630–3640.
- Létang J-M, Freud N, Peix G. Signal-to-noise ratio criterion for the optimization of dual-energy acquisition using imaging virtual x-ray. *J Electron Imaging.* 2004;13:436.
- Bethesda M. ICRU Report N. 46: Photon, Electron, Proton and Neutron Interaction Data for Body Tissues, Tech. Rep.; 1992.
- Berger MJ, Coursey JS, Zucker MA, Chang J. *ESTAR, ASTAR, PSTAR: Stopping-Power and Range Tables for Electrons, Protons, Helium ions.* NIST. Gaithersburg, MD: National Institute of Standards and Technology; 2005. <http://www.nist.gov/pml/data/star/index.cfm>.
- Richard S, Siewersden JH. Optimization of dual-energy imaging systems using generalized NEQ and imaging task. *Med Phys.* 2007;34:127–139.
- Vilches-Freixas G, Létang J-M, Presich K, Steininger P, Rit S. Optimal dose balance between energy levels for material decomposition with dual-CT energy X-ray. *Radiat Oncol.* 2015;115:S506–S507.
- Arbor N, Dauvergne D, Dedes G, et al. Monte Carlo comparison of X-ray and proton CT for range calculations of proton therapy beams. *Phys Med Biol.* 2015;60:7585.
- Sossin A, Tabary J, Rebuffel V, et al. Inuence of scattering on material quantification using multi-energy X-ray imaging. *Proc IEEE Nucl Sci Symp Med Imaging Conf.* 2014;0:1–5.